Visualizing the Subsurface of Soft Matter: Simultaneous Topographical Imaging, Depth Modulation, and Compositional Mapping with Triple Frequency Atomic Force Microscopy

Daniel Ebeling,* Babak Eslami, and Santiago De Jesus Solares*

Department of Mechanical Engineering, University of Maryland, College Park, Maryland 20742, United States

ABSTRACT Characterization of subsurface morphology and mechanical properties with nanoscale resolution and depth control is of significant interest in soft matter fields like biology, polymer science, and even in future applications like nanomanufacturing, where buried structural and compositional features are important to the functionality of the system. However, controllably "feeling" the subsurface is a challenging task for which the available imaging tools are relatively limited. In this paper, we propose a trimodal atomic force microscopy (AFM) imaging scheme, whereby three eigenmodes of the microcantilever probe are used as separate control "knobs" to simultaneously measure the topography, modulate sample indentation by the tip during tip–sample impact, and map compositional contrast, respectively. We illustrate this multifrequency imaging approach through computational simulation and experiments conducted on ultrathin polymer films with embedded glass nanoparticles in ambient air. By actively increasing the tip–sample indentation using a higher eigenmode of the cantilever, we are able to gradually and controllably reveal glass nanoparticles which are buried tens of nanometers deep under the surface, while still being able to refocus on the surface.

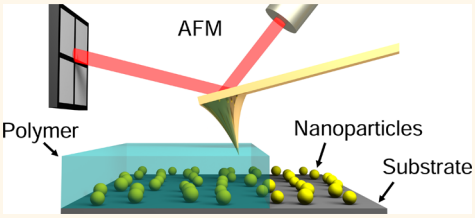

KEYWORDS: atomic force microscopy · indentation · soft matter · stiffness · multimodal · amplitude modulation · frequency modulation

Atomic force microscopy (AFM[1]), developed in the mid-1980s, has become a widely used tool for measuring topography and probe-sample forces on micro- and nanoscale surfaces. Since the introduction of the original method, more sophisticated variations have been developed which offer new capabilities. One of these variations is multifrequency AFM, which was introduced by Garcia and coworkers in 2004 for noncontact amplitude-modulation applications in air and later extended to repulsive contact and liquid environments.[2–9] The underlying concept consists of mapping the phase of one higher eigenmode of the cantilever, which is excited with constant drive amplitude and frequency, simultaneously while the fundamental eigenmode is used to carry out topographical imaging through the standard amplitude-modulation (AM) method.[10] The oscillation amplitude of the higher eigenmode is significantly smaller than that of the fundamental mode, and can be varied independently of the topographical controls scheme. This allows the probe to explore a wider range of tip–sample interactions while mapping the compositional contrast of the surface through the phase shift. There exist a number of other multifrequency and multiharmonic imaging techniques which have also been introduced recently, each having its own application niche.[11–17]

The multifrequency concept of Garcia and co-workers (henceforth referred to AM-OL, since it is the combination of AM for the fundamental mode and an open-loop (OL) drive for the higher mode) was subsequently extended to frequency modulation (FM) imaging in ultrahigh vacuum by Meyer and co-workers[18] and to a combination of

* Address correspondence to debeling@umd.edu, ssolares@umd.edu.

Received for review September 16, 2013 and accepted October 9, 2013.

Published online October 17, 2013
10.1021/nn404845q

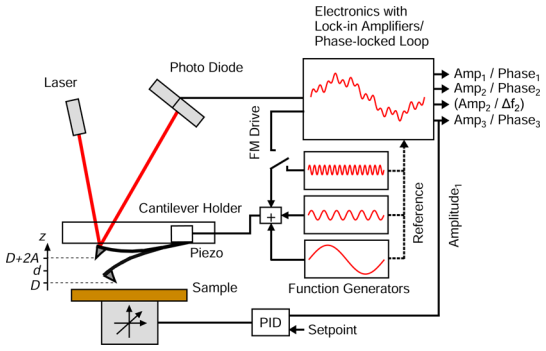

Figure 1. Schematic layout of the setup used. The cantilever is excited at the frequencies of three different eigenmodes simultaneously. In the simplest case (AM-OL-OL), this can be accomplished by adding the drive signals of three function generators. In this case, the oscillation signal from the photo diode can be read by three separate lock-in amplifiers to determine the amplitudes and phase shifts of the corresponding eigenmodes. For the more sophisticated cases (AM-FM-OL or AM-OL-FM), one of the drive signals from the function generators has to be replaced by an appropriate FM driving signal, *e.g.*, from a phased-locked loop (PLL) electronics. In this case, the PLL is used to determine the frequency shift of the oscillation signal and either its response or drive amplitude. The first eigenmode oscillation amplitude is used as an input signal for the tip-sample distance feedback.

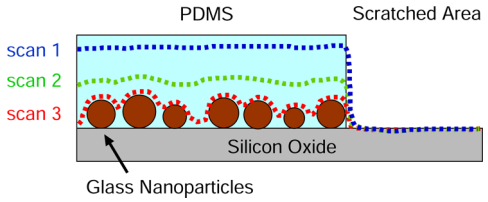

Figure 2. Practical illustration of sample scans performed at varying tip penetration depth for a sample having subsurface features. Such modulation of the indentation depth can be achieved simultaneously with topographical imaging and compositional mapping through trimodal AFM. The depicted sample setup consists of a thin polydimethylsiloxane (PDMS) layer (several tens of nanometers in thickness) which was spin-coated onto a silicon wafer that had been previously coated with glass nanoparticles. By removing parts of the PDMS film *via* scratching, the bare silicon oxide surface can be used as a height reference.

AM and FM by us, in which the fundamental mode was used to map the topography, as in AM-OL, while a higher eigenmode was driven using FM for compositional contrast (this method is henceforth referred to as AM-FM[19−22]). We further implemented a trimodal scheme (either AM-OL-FM, AM-FM-OL or AM-OL-OL;[19,20] see Figure 1 for a schematic of the instrumentation) which was shown to be stable for imaging in air. We also showed that the measured observables for different eigenmodes agreed qualitatively with one another. For example, we showed mathematically, computationally, and experimentally that the phase contrast obtained for higher eigenmodes driven with OL is qualitatively antiparallel to the frequency shift contrast obtained for higher eigenmodes driven with FM (this is true both in bimodal[21,22] and trimodal[19,20] operation).

While the benefits of the bimodal scheme of Garcia and co-workers (and any variants of it) were immediately evident in that it offered two relatively weakly coupled control "knobs" that the user could manipulate in order to optimize topographical imaging and compositional contrast mapping, respectively, it was not clear whether our trimodal scheme could offer any additional benefits. That is, it was not clear whether one could use a third eigenmode as a new control knob that would allow the user to manipulate an additional aspect of sample characterization. Besides, the instrumentation required to implement the trimodal controls is more elaborate, for obvious reasons, and the method was also shown to have potential operational disadvantages. Specifically, we showed in ref 20 that (i) the three eigenmodes can perturb one another to a greater or lesser degree, depending on the imaging conditions and sample type; (ii) the use of higher eigenmodes significantly increases the depth to which the cantilever tip penetrates into the sample during every tap, leading to different results depending on how many eigenmodes are driven and what their amplitudes are; and (iii) the cantilever tip oscillation is such that not all tip−sample impacts are equal, thus leading to an imaging process in which the cantilever response never reaches a true steady state.

In this work, we leverage the previous features of the bimodal and trimodal methods in implementing a trimodal scheme which offers separate knobs for optimizing topographical imaging, sampling depth and compositional contrast, respectively. In other words, we optimize each eigenmode for a different purpose. The first eigenmode settings are optimized for topographical imaging as in standard tapping-mode AFM. The second eigenmode is used for compositional mapping as in the methods of Garcia and coworkers. Finally, the third eigenmode is driven with increasingly larger amplitude which increases tip penetration and in some cases leaves the surface temporarily indented, thus revealing buried features. As illustrated schematically in Figure 2, this method can be useful for studying samples having subsurface features, which the user can characterize by performing scans at varying sampling depths. An interesting field of application for this technique could be, for example, probing the distribution or alignment of nanosized particles in new composite materials. One of the first applications of carbon nanotubes was, for instance, modifying the mechanical properties of composite materials (see, *e.g.*, ref 23 and refs therein). Also other kinds of nanoparticles have been shown to improve the material properties of a variety of composites (see, *e.g.*, ref 24). Our proposed method is able to add a significant contribution in further studying and rendering these new materials since it offers a way to locate and mechanically characterize these subsurface structures with lateral resolution in the nm regime. Other

important areas which can profit from subsurface imaging are, for example, biological and medical applications. Nanomaterials have found their way into a fairly broad range of clinical applications, and topics like biocompatibility and toxicity of nanosized compounds are frequently discussed (see, *e.g.*, ref 25 and refs therein). It is also often necessary to study the subsurface of biological matter (*e.g.*, the inside of cells) to detect the presence and distribution of organelles and nanomaterials.[26] Different methods have been used in the past to tackle the task of analyzing buried structures. Most commonly, scanning or transmission electron microscopy is used nowadays for this purpose (see, *e.g.*, refs 27 and 28). However, a few scanning probe microscopy based subsurface detection techniques have also been established, which range from electrical detection,[29−31] ablation-based methods,[32] and ultrasonic wave detection,[33−39] to spectroscopy based methods.[40,41] Our approach joins this young family of subsurface force microscopies bringing added flexibility, relative ease of use, and short characterization time.

We illustrate the concepts and application of the technique through simulation and experiments. For the sake of brevity, we do not repeat the intricacies of previously reported methods (by us and by others), except when this is necessary to understand the proposed approach.

PROPOSED TRIMODAL IMAGING STRATEGY

The proposed imaging concept consists in using three different eigenmodes as separate control knobs to (i) optimize topographical imaging (fundamental eigenmode), (ii) modulate tip penetration depth (a high eigenmode), and (iii) map compositional contrast (a very sensitive eigenmode, lower than the one used for depth modulation). For example, if the first three eigenmodes are driven, the third eigenmode would be used to modulate tip penetration, while the second eigenmode would be used to map compositional contrast (the fundamental mode would of course be used for topographical imaging). The compositional mapping eigenmode can be driven either in OL or FM (see ref 22 for a comparison).

The selection of the highest driven eigenmode for regulating tip penetration can be justified by inspecting the dimensionless equation of motion of a damped harmonic oscillator.[21,22,42−44]

$$\frac{d^2\bar{z}}{d\bar{t}^2} = -\bar{z} + \frac{1}{Q}\left(-\frac{d\bar{z}}{d\bar{t}} + \cos(\bar{t})\right) + \frac{F_{ts}(\bar{D})}{kA_0} \qquad (1)$$

Here A_0 is the free oscillation amplitude, $\bar{z}(t) = z(t)/A_0$ is the dimensionless tip position with respect to the cantilever base position, $\bar{D}(t) = D(t)/A_0$ is the dimensionless tip−sample distance (in the above equation, $D(t) = d(t) + z(t)$, where d is the cantilever base position with respect to the sample surface, see Figure 1), $\bar{t} = \omega_0 t$ is the dimensionless time, k is the cantilever force constant (stiffness), and F_{ts} is the tip−sample interaction force. We have also used the approximation $A \approx A_0 = F_0Q/k$,[10] where F_0 is the amplitude of the excitation force, and have grouped the damping and excitation terms together in brackets with the coefficient $1/Q$, where Q is the quality factor. It can be inferred from the last term on the right-hand side of this equation that the tip−sample forces are normalized by the product of the force constant times the free oscillation amplitude, such that the external force term becomes more or less relevant to the dynamics when the product kA_0 becomes smaller or larger, respectively. Since the cantilever becomes more sensitive to external forces when this term becomes more dominant, sensitivity increases with decreasing amplitude. As the product kA_0 decreases, the oscillator is more easily perturbed by the tip−sample forces, whereas the perturbations are less significant when this product increases. In the present method, one wishes to have a knob that can easily increase tip−sample penetration, so one chooses the highest driven eigenmode, which has the highest dynamic force constant and thus the largest product kA_0.

Figure 3 shows simulations which illustrate that the gain in tip−sample penetration is greatest for the highest eigenmodes, in agreement with eq 1. This figure also illustrates that penetration can be increased by increasing the amplitude of any eigenmode, even the fundamental (see also refs 45−47 for seminal studies on viscoelastic sample response and increased tip−sample indentation of compliant materials in single mode AFM). However, the gain in penetration is greater for the higher eigenmodes. Figure 3 shows only curves generated for bimodal cases, but we also analyzed cases where all three eigenmodes are excited (not shown), which reveal qualitatively similar trends. Figure 4 shows simulated amplitude and phase curves *vs* cantilever position for three different combinations of amplitudes for the first three eigenmodes, also illustrating that the highest eigenmode is the least sensitive to the tip−sample forces. This can be inferred from the fact that the amplitude and phase of the third eigenmode (red trace) vary the least when the cantilever is lowered toward the sample, in comparison to the amplitude and phase of the other two eigenmodes.

In agreement with the arguments above, the user should choose the lowest possible higher eigenmode that can be controllably driven for carrying out compositional contrast mapping (the fundamental mode is still reserved for topographical imaging, since it has the lowest frequency and thus controls the number of sample impacts per unit of time). This is because here one wishes to use a highly sensitive eigenmode for this purpose. Figure 4 illustrates that the second eigenmode is much more sensitive to the presence of the sample than the third one, which makes it more

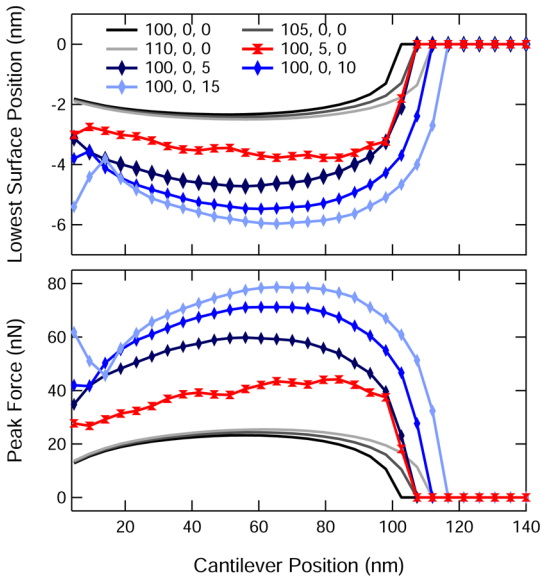

Figure 3. Computational results illustrating increased tip penetration depth when higher eigenmodes are active. The traces are labeled with the amplitude used of the first three eigenmodes and the legend is the same for both graphs. For example, "105, 5, 0" means that the free oscillation amplitudes of these eigenmodes were 105, 5, and 0 nm, respectively. The graph also shows that penetration changes with changes in cantilever position are not as smooth with the second eigenmode as they are for the third and first modes. This is because the tapping frequency of the third eigenmode is higher, leading to a more regular impact, closer to the behavior of a single frequency impact. The surface parameters used for this simulation (see Figure 8a in Methods section) were $K_0 = K_{inf} = 10$ N/m and $C_d = 1 \times 10^{-5}$ Ns/m. The cantilever parameters were $k_1 = 4$ N/m, $Q_1 = 150$, $f_1 = 75$ kHz, $Q_2 = 3Q_1$, $Q_3 = 5Q_1$, $f_2 = 6.25f_1$, $f_3 = 17.6f_1$. The higher mode force constants were adjusted through the relationship $k_i = k_1(f_i/f_1)^2$.

suitable for mapping compositional contrast. The control knob in this case, which tunes its ability to map material properties, is this eigenmode's free amplitude, which as Figure 4 shows, directly influences its sensitivity. Again, the eigenmode becomes more sensitive (*i.e.*, it is more easily perturbed by the presence of the sample) as its amplitude decreases. The effect of the amplitude is further illustrated in Figure 5, which schematically shows the free and engaged amplitude and phase response of a higher eigenmode for three different free oscillation amplitudes (experimentally these curves can be constructed by sweeping the drive frequency of the higher eigenmode while observing its response phase and amplitude when the sample is engaged and when it is not engaged). In the first case (a and b, largest amplitude), the eigenmode is not significantly perturbed upon engaging the sample, leading to a very small change in the phase and amplitude, in turn leading to low sensitivity characterization: the magnitude of the response variables, phase and amplitude *shift*, is very small and may thus be hard to detect. In the second case (c and d), the smaller free amplitude leads to a greater perturbation of the eigenmode, which in turn results in a greater change in its response variables, making the characterization more sensitive: the magnitude of the observables is greater and so is their rate of change (*i.e.*, the slope of the phase and amplitude *vs* frequency curves at the vertical red dashed line). In the third case (e and f), the free amplitude has been reduced further, which further enhances the perturbation and makes the eigenmode even more sensitive, although this is not necessarily

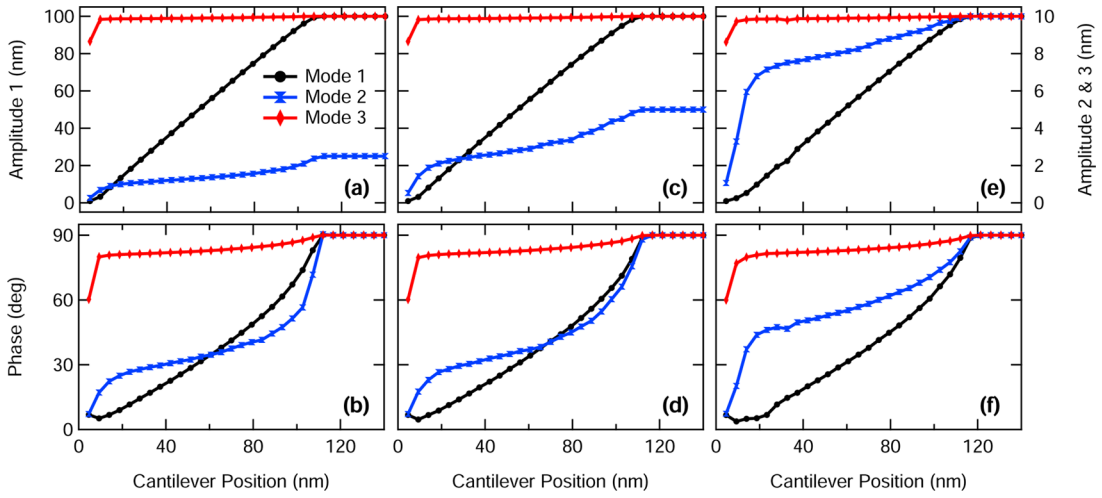

Figure 4. Numerical simulation results illustrating modulation of the sensitivity of the compositional mapping eigenmode (second eigenmode in this case, see also Figure 5): amplitude and phase for eigenmode amplitudes of 100, 2.5,10 (a and b, respectively), 100, 5, 10 (c and d, respectively) and 100, 10, 10 (e and f, respectively). Note that in the top row the trace for the first mode is plotted on the left axis, while the traces for modes 2 and 3 are plotted on the right axis. The results show that the third eigenmode (red trace) is highly insensitive to the change in cantilever distance with respect to the sample for the sample selected. The second eigenmode (blue trace) is highly sensitive to the presence of the surface for the selected amplitudes and becomes more sensitive as its amplitude decreases, in agreement with eq 1. The higher sensitivity for decreasing free amplitude can be seen in the steeper change in the phase upon initial approach toward the sample (the blue trace drops below the other two traces as the second eigenmode free amplitude decreases). The surface and cantilever parameters are the same as for Figure 3. The legend is the same for all graphs.

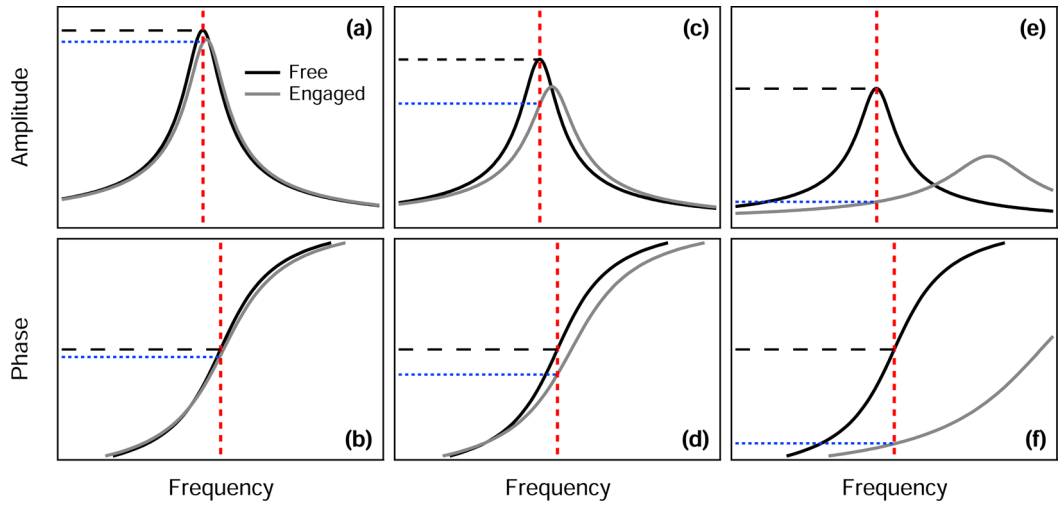

Figure 5. Conceptual illustration of sensitivity optimization for the compositional eigenmode. Each column illustrates a separate "experiment"" using a different free oscillation amplitude, with the top row describing the free (away from the sample) and engaged amplitude-frequency response of the eigenmode and the bottom row describing the corresponding phase-frequency responses: large amplitude (a and b), medium amplitude (c and d) and small amplitude (e and f). The dashed horizontal black line indicates the amplitude and phase values for free oscillation of the eigenmode driven at the resonance frequency, while the dotted horizontal blue line indicates the engaged values for the same variables at the same drive frequency. The perturbation of the eigenmode dynamics becomes more significant as the amplitude decreases, in agreement with Figure 4 and eq 1. Further details on the amplitude and phase response of higher modes in multifrequency imaging can be found in our previous studies.[20,22] The legend is the same for all graphs.

desirable. If the compositional eigenmode is driven in OL, the latter situation would be undesirable because although the phase and amplitude shifts are large (which makes them more easily detectable), they fall in the regions where the respective curves are flatter, such that changes in the nature of the sample lead to smaller changes in the observables. In contrast, if the eigenmode is driven in FM, it may be desirable to have the larger frequency shift, although if the frequency and amplitude shift are excessive, this may also lead to instabilities in the controls scheme. Further discussion on these topics can be found in refs 20 and 22.

EXPERIMENTAL IMPLEMENTATION AND DISCUSSION

To evaluate the proposed method, we performed AFM imaging experiments on soft polydimethylsiloxane (PDMS) films with embedded glass nanoparticles (see Figure 2 for an illustration of the sample setup). The soft PDMS films are spin coated onto hard silicon oxide substrates. After scratching parts of the PDMS film away, the silicon substrate serves as a reference height during the measurement. Figure 6 shows AM-OL-OL AFM measurements where we used the first eigenmode of the cantilever for imaging the topography, the second eigenmode for obtaining compositional contrast and the third eigenmode for actively adjusting the peak tip−sample indentation. The images in the three columns are measured for three different amplitudes of eigenmode 3 (*amp*3 = 0, 9, and 27 nm, from left to right), while all other imaging parameters, especially the free amplitudes of eigenmode 1 and 2 and the imaging set point, were kept constant. The first row depicts the measured topography information, whereas the subsequent rows show the phase shift images for the three eigenmodes. The PDMS film can be found on the left side of each image (yellow colors in height and phase images), and the silicon substrate is located on the right side (dark brown regions in topography images and violet regions in phase images). These darkest regions serve as a reference height for our topography measurements.

It is evident in the topography images (first row) that the measured height of the PDMS layer decreases with increasing third eigenmode amplitude resulting in darker colors for the PDMS film for each subsequent image (from left to right). This reduction in measured height directly reflects the higher tip−sample indentation when increasing the highest eigenmode's amplitude as described in the previous section. On the right side of the topography image for *amp*3 = 0 nm (left column), it can be seen that the silicon substrate is not completely free of soft material after scratching. This is confirmed by the corresponding phase image which shows yellow (*i.e.*, soft in this case) regions over the scratched portion of the surface. The images in the middle and right columns reveal that these soft regions on the silicon substrate seem to vanish with increasing third eigenmode amplitude. This is explained by the fact that the remaining soft material gets increasingly compressed with higher tip−sample indentation and the tip starts "feeling" the underlying hard substrate. Furthermore, it is noticed that the PDMS films look smooth and almost featureless for *amp*3 = 0 and 9 nm, whereas multiple features appear below the surface for *amp*3 = 27 nm. In this case of the highest

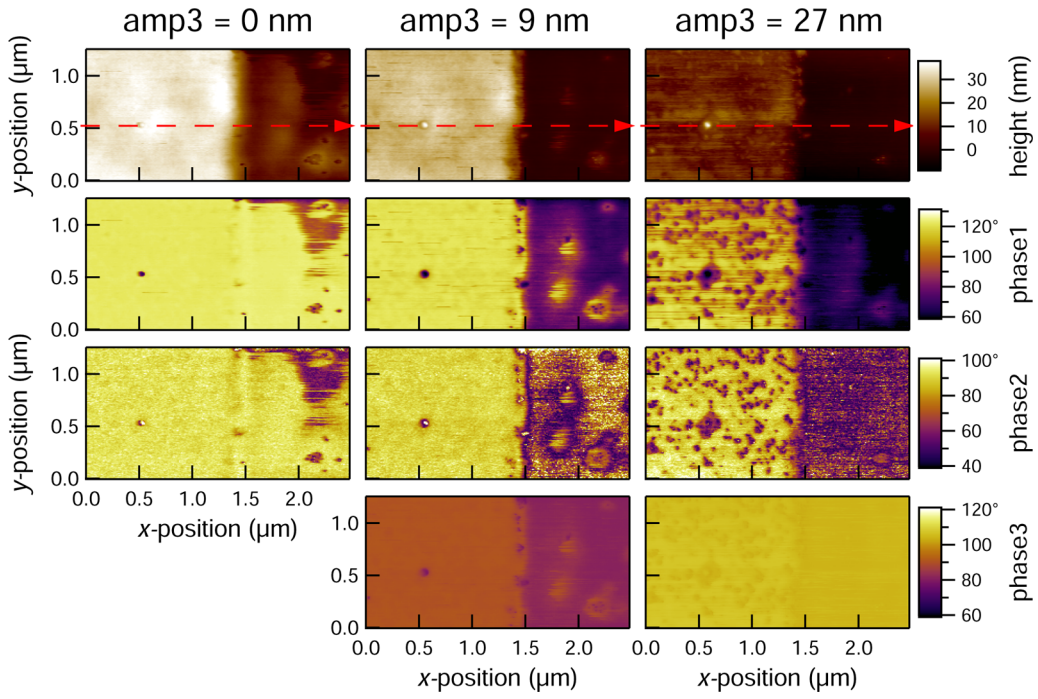

Figure 6. AFM images measured on a soft PDMS film which is supported by a hard silicon oxide substrate. In the right part of the images, the PDMS film was scratched away to expose the bare silicon oxide surface. The top row shows topography images for three different free third eigenmode amplitudes. The corresponding phase images for all three eigenmodes are depicted in the subsequent rows. Imaging parameters: A_{1free} = 126 nm, amplitude set point ratio = 0.6, A_{2free} = 1 nm. Cantilever parameters: Cont40A (MPP-33120, Bruker), k_1 = 2.7 N/m, Q = 165, f_1 = 42.2 kHz, f_2 = 264.7 kHz, f_3 = 738.8 kHz. Through the relationship $k_i = k_1(f_i/f_1)^2$, the higher mode force constants can be approximated as k_2 = 106 N/m and k_3 = 830 N/m.

third eigenmode amplitude, the AFM tip indents so deep into the PDMS film during each oscillation cycle of the first eigenmode that it is able to sense the glass nanoparticles which are embedded in the film. This effect is most impressive when comparing the images of the second eigenmode phase channel (third row) which provide the highest lateral contrast.

Figure 7 depicts single topography (top graph) and second eigenmode phase (bottom graph) scan lines which were taken from the corresponding images in Figure 6 (positions marked with red arrows). These scan lines reveal a decreasing measured average height of the PDMS films from ≈34 nm (blue line) to ≈28 nm (green line) to ≈10 nm (red line) for increasing third mode amplitudes. In the corresponding phase scan lines, the parts of the surface which are covered by PDMS can be clearly distinguished form uncovered parts by comparatively higher phase values ($\Delta\Phi \approx 40°$ between the PDMS and the silicon oxide surface). Interestingly, in the red and green topography scan lines as well as in all three phase scan lines, a single feature is visible (at an x-position of ≈0.6 μm) which is caused by an agglomeration of glass beads. The height of this feature (≈36 nm) is close to the measured average height of the PDMS film under conditions with *amp*3 = 0 nm. Except for this single feature, the phase scan lines for the two lowest third eigenmode amplitudes (blue and green curves) do not show any other features within the PDMS film (compare to the smooth

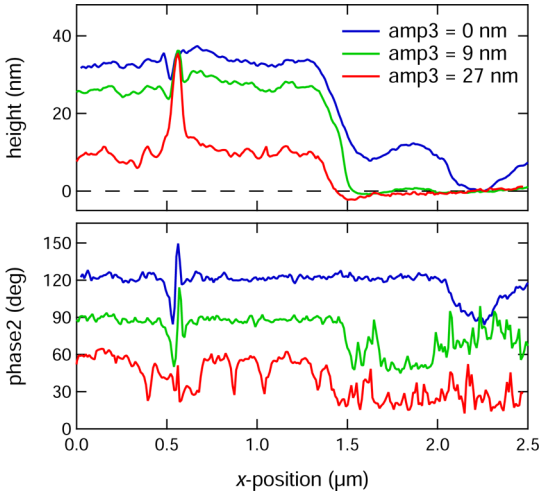

Figure 7. Single scan lines taken from images in Figure 6 (positions of the scan lines are indicated in Figure 6 by red arrows). Top graph: topography scan lines for three different third eigenmode amplitudes (scan lines are slightly shifted in x and z-directions to match sample drift and adjust for the same reference height (silicon surface), respectively). Bottom graph: corresponding scan lines showing the phase shift of the second eigenmode (for better visibility the blue and red curves are shifted by ±30 deg.).

appearance of the PDMS film in the second eigenmode phase images in Figure 6 third row). However, in the case of the highest third eigenmode amplitude (red curve), the phase scan lines (and images in Figure 6) are

littered with peaks and potholes in the region of the PDMS film which are caused by underlying single glass nanoparticles. Under these conditions, the PDMS film is compressed so strongly that even single glass nanoparticles (average diameter 13.7 ± 2 nm) become visible. To unambiguously confirm that the imaged features are caused by embedded glass nanoparticles, we performed a control experiment where a sample with glass beads is directly compared to a sample without embedded features (see Supporting Information Figure S1). Indeed the features are only observed on the sample with embedded nanoparticles under high indentation imaging conditions.

The behavior found for the PDMS films under the imaging conditions examined was fully reversible, meaning that we could not observe any permanent deformations of the PDMS film after reducing the indentation forces again. Nevertheless, we have observed that imaging with high indentation forces for prolonged periods can result in blunting of the AFM tips for our samples. We believe that this effect is increased in our measurements since ≈1/3 of the imaging area was not covered by PDMS in order to have the silicon oxide surface as a reference height. Tapping with the AFM tip on this rather hard surface during "high indentation" imaging conditions increases the wear of the tip significantly. However, for most applications the presence of a hard reference surface will not be needed which will reduce the tip wear.

The measurements presented show unambiguously that the proposed imaging strategy of using a higher eigenmode to increase the tip−sample indentation is able to detect nanometer sized subsurface features which are buried in softer matrices. Since the method utilizes tip oscillations in the normal direction with high frequencies (on the order of 100 oscillations of the first eigenmode per imaging pixel), increasing the tip−sample indentation in the proposed way should not result in increased lateral forces during scanning of the surface. This is a clear advantage in comparison to increasing the loading force in contact mode operation which will result in significant tearing/damaging of the sample surface. Comparing the method to previously introduced subsurface techniques which also rely on mechanical indentation of the sample surface (spectroscopy based methods[40,41]) our approach is capable of achieving the desired information during the standard imaging process without the need for relatively slow "force volume scanning" or complex offline data analysis.

Additionally, the presence of separate control "knobs" in trimodal AFM enriches the experimentalist with options for finding the best imaging conditions. Having the ability to choose between different free amplitudes for the different eigenmodes as well as amplitude set points for the tip−sample distance feedback allows the user to adjust the imaging mode for a large variety of relevant samples types. As an example, harder or more "sticky" samples might require higher first eigenmode amplitudes, while softer samples or samples with less attractive forces could be adequately imaged with smaller amplitudes, *etc.* In both cases, however, the higher eigenmode parameters can be varied independently to optimize peak indentation and compositional contrast.

In this work, we have used AM-OL-OL AFM, which is the simplest and most stable of the different triple frequency operation modes. It has been previously shown that stable imaging is also possible while exciting one eigenmode with the FM technique (AM-FM-OL or AM-OL-FM operation),[19,20] so these modes could be used for the proposed method as well. However, here we are focusing on AM-OL-OL operation for increasing the tip−sample indentation by using a higher eigenmode since the discernment of FM *vs* OL operation is not the object of this paper.

We do point out that the compositional mapping (in our case through the second eigenmode images) does *not* necessarily reveal *quantitative* material information. Reasons for this are that the penetration of the tip into the sample surface is neither uniform nor controlled, tip−sample forces are nonlinear, and the observables are averages over multiple of oscillation cycles, *etc.* Nevertheless, the method offers a convenient way for mapping the surface and subsurface and obtaining material contrast *easily, rapidly* and without excessive sample damage.

As in every AFM experiment, the lateral resolution of the method is determined primarily by the radius of the tip apex. In general, the lateral resolution which can be achieved using the method when imaging subsurface features is poorer than in the case where the glass beads are not embedded into a polymer matrix. For the data shown in Figures 6 and 7 the lateral resolution for the buried nanoparticles is on the order of 30 nm, since two single glass beads can still be distinguished in the second eingenmode phase images if they are separated by this distance.

Since the depth of single impacts of the tip into the sample surface are not equal in trimodal AFM (see Figure 8e which shows that not every oscillation reaches the deepest sampling points), it may be necessary in some cases to reduce the sampling frequency of the signals, which may limit the maximum possible scan speed. For the data shown here we were sampling at a rate of 512 image pixels per second and the frequency of the first eigenmode was 42 kHz. This corresponds to over 80 tip−sample impacts per pixel, ensuring a reasonable amount of averaging.

Finally, we note that the theoretical model, which was used to describe the effects of increasing or decreasing higher eigenmode amplitudes, does not contain specific types of forces which may play an

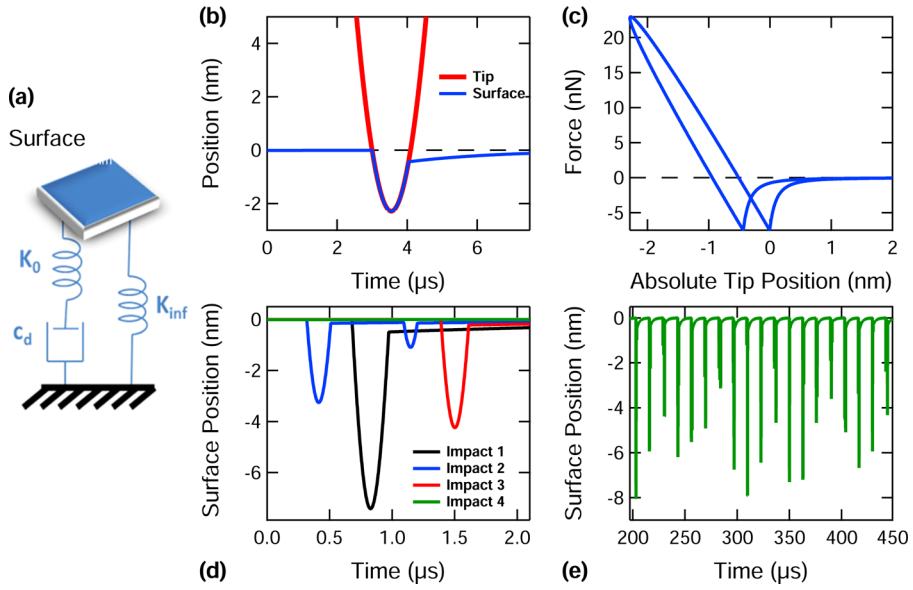

Figure 8. Standard linear solid tip−sample interaction model: (a) mechanical model (K_0 and K_{inf} are linear springs and C_d is a linear damper); (b) illustration of AFM tip and surface trajectory during single-frequency AFM impact (notice how the surface remains indented and recovers gradually after the tip leaves); (c) force *vs* tip position for the impact shown in (b); (d) illustration of surface trajectory for successive multifrequency AFM impacts (the trajectories of successive impacts are time-shifted by whole cantilever periods in order to plot them on top of one another), showing how each impact differs from the previous one (notice how they generally exhibit appreciably greater penetration than for the single frequency case); (e) illustration of a large number of successive multifrequency AFM surface trajectories as a function of time. Remarkably, the phase and amplitude of all driven eigenmodes can reach steady values despite the variability in the impacts.

important role during the imaging process, like, *e.g.*, adhesion, thin-fluid-film forces, *etc.* Although these types of force are not considered in a specific way, the general outcome of our dimensional analysis covers them all since the importance of the force term F in eq 1 to the dynamics is modulated by the product kA regardless of what the forces are.

CONCLUDING REMARKS

We have presented a new trimodal imaging strategy that can be applied to detect and image features that are buried tens of nanometers under the sample surface with nanoscale lateral resolution. By using three different oscillation eigenmodes of the AFM cantilever, one can obtain topographical and compositional information of the sample surface simultaneously, and in addition actively change the tip−sample indentation. It has been shown theoretically as well as experimentally that by adjusting the different control "knobs" of the proposed method (*i.e.*, free amplitudes of different cantilever eigenmodes) each of the chosen eigenmodes can be tailored to serve a separate purpose, namely, topographical imaging, compositional contrast mapping, and tip-sample indentation control. This capability can be adequately explained by analyzing a dimensionless version of the equation of motion of a harmonic oscillator.

The method presented can offer a significant contribution to a wide range of applications in materials science, biology, and many nanoscale applications where the subsurface structure plays an important role. Specifically, the technique serves as a versatile tool for "touching" and observing the surface and subsurface of the sample in its pristine form, without requiring complex surface preparation procedures to enable "a look at the inside".

METHODS

Simulation Methods. For our numerical simulations three eigenmodes of the AFM cantilever were modeled using individual equations of motion for each, coupled through the tip−sample interaction forces as in ref 20. Each eigenmode was driven using a sinusoidal base excitation of constant amplitude and frequency equal to its natural frequency. The equations of motion were integrated numerically and the amplitude and phase of each eigenmode were calculated using the customary in-phase and quadrature terms. The repulsive tip−sample forces were introduced through a standard linear solid (SLS) model (Figure 8a), which is the simplest representation that can reproduce both stress relaxation and creep compliance.[48] Both of these behaviors are observed in the response of real viscoelastic surfaces, which can remain deformed following temporary indentation and gradually recover upon stress release. This temporary deformation and gradual recovery is illustrated in Figure 8b and a typical force curve for single-frequency tip−sample impacts for a SLS surface is shown in Figure 8c. Figure 8d,e shows successive multifrequency tip−sample impacts, which have previously been shown to differ considerably for different cantilever oscillations.[20] The attractive forces were modeled through the standard van der Waals term generally used in AFM simulation,[10] which is included in the calculations of Figure 8b−e.

Sample Preparation. Silicon wafers (Ted Pella, Inc.) were rinsed with isopropyl alcohol, ethanol, and DI-water (Sigma Aldrich) before heating them with a butane torch (until bright orange glowing) for ≈30 s. Subsequently, the silicon surface was coated with glass nanoparticles (size = 13.7 ± 2 nm, Microspheres-Nanospheres; Corpuscular, Inc.) by the drop casting method. For this the original nanobead solution was diluted with DI-water to a concentration of 1%. A small droplet (20 μL) of this solution was dropped onto the silicon oxide surface and allowed to incubate for ≈1 min before the surface was thoroughly blow dried with air. The PDMS (Sylgard 184, Sigma Aldrich) was diluted with hexane (Sigma Aldrich) to achieve ultrathin films as described in ref 49. The final mixing ratio was *PDMS curing agent/PDMS base/hexane* = 1:10:1000 (by weight). This solution was spin-coated at 6000 rpm onto the silicon wafer pieces (≈ 1 × 1 cm^2) for 180 s. Finally, the PDMS films were cured on a hot plate at 150 °C for 10 min. Before the samples were placed into the AFM, a line was gently scratched into the film with sharp tweezers to expose portions of the silicon oxide surface.

AFM Measurements. A commercial instrument (Asylum Research, MFP3D) was equipped with an external electronics (RHK Technologies, PLL Pro) to drive the cantilever at three eigenmodes simultaneously in the AM-OL-OL mode. A scheme of the system setup used can be found in Figure 1. The AFM tips used (Cont40A, MPP-33120, Bruker) were rinsed prior to experiments with isopropyl alocohol, ethanol, and DI-water. First, the free amplitude and amplitude set point of the first eigenmode were set to values for which stable imaging of the surface was possible. Subsequently, we adjusted the drive amplitudes of the second and third eigenmodes to achieve compositional mapping and the desired amount of tip−sample indentation, respectively. We increased and decreased the third eigenmode amplitude step by step for obtaining images with higher and lower tip−sample indentation several times to check whether the imaging procedure permanently damages the sample surface.

Conflict of Interest: The authors declare no competing financial interest.

Acknowledgment. The authors gratefully acknowledge support from the U.S. Department of Energy (conceptual method development and experimental work, award DESC-0008115) and the U.S. National Science Foundation (computational work, award CMMI-0841840). We also thank Ying Liu and Dr. Chunsheng Wang for sharing their spin-coating device.

Supporting Information Available: Figure S1 provides the results of a control experiment with and without subsurface features. This material is available free of charge *via* the Internet at http://pubs.acs.org.

REFERENCES AND NOTES

1. Binnig, G.; Quate, C.; Gerber, C. Atomic Force Microscope. *Phys. Rev. Lett.* **1986**, *56*, 930–933.
2. Rodriguez, T.; Garcia, R. Compositional Mapping of Surfaces in Atomic Force Microscopy by Excitation of the Second Normal Mode of the Microcantilever. *Appl. Phys. Lett.* **2004**, *84*, 449–451.
3. Martinez, N. F.; Patil, S.; Lozano, J. R.; Garcia, R. Enhanced Compositional Sensitivity in Atomic Force Microscopy by the Excitation of the First Two Flexural Modes. *Appl. Phys. Lett.* **2006**, *89*, 153115.
4. Lozano, J. R.; Garcia, R. Theory of Multifrequency Atomic Force Microscopy. *Phys. Rev. Lett.* **2008**, *100*, 076102.
5. Martinez, N. F.; Lozano, J. R.; Herruzo, E. T.; Garcia, F.; Richter, C.; Sulzbach, T.; Garcia, R. Bimodal Atomic Force Microscopy Imaging of Isolated Antibodies in Air and Liquids. *Nanotechnology* **2008**, *19*, 384011.
6. Lozano, J. R.; Garcia, R. Theory of Phase Spectroscopy in Bimodal Atomic Force Microscopy. *Phys. Rev. B* **2009**, *79*, 014110.
7. Garcia, R.; Herruzo, E. T. The Emergence of Multifrequency Force Microscopy. *Nat. Nanotechnol.* **2012**, *7*, 217–226.
8. Proksch, R. Multifrequency, Repulsive-Mode Amplitude-Modulated Atomic Force Microscopy. *Appl. Phys. Lett.* **2006**, *89*, 113121.
9. Stark, R. W. Dynamics of Repulsive Dual-Frequency Atomic Force Microscopy. *Appl. Phys. Lett.* **2009**, *94*, 063109.
10. Garcia, R.; Perez, R. Dynamic Atomic Force Microscopy Methods. *Surf. Sci. Rep.* **2002**, *47*, 197–301.
11. Stark, M.; Stark, R.; Heckl, W.; Guckenberger, R. Inverting Dynamic Force Microscopy: From Signals to Time-Resolved Interaction Forces. *Proc. Natl. Acad. Sci. U.S.A.* **2002**, *99*, 8473–8478.
12. Sahin, O.; Magonov, S.; Su, C.; Quate, C. F.; Solgaard, O. An Atomic Force Microscope Tip Designed to Measure Time-Varying Nanomechanical Forces. *Nat. Nanotechnol.* **2007**, *2*, 507–514.
13. Platz, D.; Tholen, E. A.; Pesen, D.; Haviland, D. B. Intermodulation Atomic Force Microscopy. *Appl. Phys. Lett.* **2008**, *92*, 153106.
14. Li, Y. J.; Takahashi, K.; Kobayashi, N.; Naitoh, Y.; Kageshima, M.; Sugawara, Y. Multifrequency High-Speed Phase-Modulation Atomic Force Microscopy in Liquids. *Ultramicroscopy* **2010**, *110*, 582–585.
15. Jesse, S.; Kalinin, S. V.; Proksch, R.; Baddorf, A. P.; Rodriguez, B. J. The Band Excitation Method in Scanning Probe Microscopy for Rapid Mapping of Energy Dissipation on the Nanoscale. *Nanotechnology* **2007**, *18*, 435503.
16. Guo, S.; Solares, S. D.; Mochalin, V.; Neitzel, I.; Gogotsi, Y.; Kalinin, S. V.; Jesse, S. Multifrequency Imaging in the Intermittent Contact Mode of Atomic Force Microscopy: Beyond Phase Imaging. *Small* **2012**, *8*, 1264–1269.
17. Rodriguez, B. J.; Callahan, C.; Kalinin, S. V.; Proksch, R. Dual-Frequency Resonance-Tracking Atomic Force Microscopy. *Nanotechnology* **2007**, *18*, 475504.
18. Kawai, S.; Glatzel, T.; Koch, S.; Such, B.; Baratoff, A.; Meyer, E. Systematic Achievement of Improved Atomic-Scale Contrast *via* Bimodal Dynamic Force Microscopy. *Phys. Rev. Lett.* **2009**, *103*, 220801.
19. Solares, S. D.; Chawla, G. Triple-Frequency Intermittent Contact Atomic Force Microscopy Characterization: Simultaneous Topographical, Phase, and Frequency Shift Contrast in Ambient Air. *J. Appl. Phys.* **2010**, *108*, 054901.
20. Solares, S. D.; Chawla, G. Frequency Response of Higher Cantilever Eigenmodes in Bimodal and Trimodal Tapping Mode Atomic Force Microscopy. *Meas. Sci. Technol.* **2010**, *21*, 125502.
21. Chawla, G.; Solares, S. D. Mapping of Conservative and Dissipative Interactions in Bimodal Atomic Force Microscopy Using Open-Loop and Phase-Locked-Loop Control of the Higher Eigenmode. *Appl. Phys. Lett.* **2011**, *99*, 074103.
22. Ebeling, D.; Solares, S. D. Bimodal Atomic Force Microscopy Driving the Higher Eigenmode in Frequency-Modulation Mode: Implementation, Advantages, Disadvantages and Comparison to the Open-Loop Case. *Beilstein J. Nanotechnol.* **2013**, *4*, 198–207.
23. De Volder, M. F. L.; Tawfick, S. H.; Baughman, R. H.; Hart, A. J. Carbon Nanotubes: Present and Future Commercial Applications. *Science* **2013**, *339*, 535–539.
24. Manias, E. Nanocomposites—Stiffer by Design. *Nat. Mater.* **2007**, *6*, 9–11.
25. Riehemann, K.; Schneider, S. W.; Luger, T. A.; Godin, B.; Ferrari, M.; Fuchs, H. Nanomedicine-Challenge and Perspectives. *Angew. Chem., Int. Ed.* **2009**, *48*, 872–897.
26. Oberdorster, G.; Oberdorster, E.; Oberdorster, J. Nanotoxicology: An Emerging Discipline Evolving From Studies of Ultrafine Particles. *Environ. Health Perspect.* **2005**, *113*, 823–839.
27. Geiser, M.; Rothen-Rutishauser, B.; Kapp, N.; Schurch, S.; Kreyling, W.; Schulz, H.; Semmler, M.; Hof, V.; Heyder, J.; Gehr, P. Ultrafine Particles Cross Cellular Membranes by Nonphagocytic Mechanisms in Lungs and in Cultured Cells. *Environ. Health Perspect.* **2005**, *113*, 1555–1560.
28. Porter, A. E.; Gass, M.; Muller, K.; Skepper, J. N.; Midgley, P. A.; Welland, M. Direct Imaging of Single-Walled Carbon Nanotubes in Cells. *Nat. Nanotechnol.* **2007**, *2*, 713–717.

29. Jespersen, T. S.; Nygard, J. Mapping of Individual Carbon Nanotubes in Polymer/Nanotube Composites Using Electrostatic Force Microscopy. *Appl. Phys. Lett.* **2007**, *90*, 183108.
30. Zhao, M.; Gu, X.; Lowther, S. E.; Park, C.; Jean, Y. C.; Nguyen, T. Subsurface Characterization of Carbon NanotubesIn Polymer Composites *via* Quantitative Electric Force Microscopy. *Nanotechnology* **2010**, *21*, 225702.
31. Cadena, M. J.; Misiego, R.; Smith, K. C.; Avila, A.; Pipes, B.; Reifenberger, R.; Raman, A. Sub-Surface Imaging of Carbon Nanotube-Polymer Composites Using Dynamic AFM Methods. *Nanotechnology* **2013**, *24*, 135706.
32. Magerle, R. Nanotomography. *Phys. Rev. Lett.* **2000**, *85*, 2749–2752.
33. Kolosov, O.; Yamanaka, K. Nonlinear Detection of Ultrasonic Vibrations in an Atomic-Force Microscope. *Jpn. J. Appl. Phys.* **1993**, *32*, L1095–L1098.
34. Yamanaka, K.; Nakano, S. Ultrasonic Atomic Force Microscope with Overtone Excitation of Cantilever. *Jpn. J. Appl. Phys.* **1996**, *35*, 3787–3792.
35. Cuberes, M.; Assender, H.; Briggs, G.; Kolosov, O. Heterodyne Force Microscopy of Pmma/Rubber Nanocomposites: Nanomapping of Viscoelastic Response at Ultrasonic Frequencies. *J. Phys. D: Appl. Phys.* **2000**, *33*, 2347–2355.
36. Shekhawat, G.; Dravid, V. Nanoscale Imaging of Buried Structures *via* Scanning Near-Field Ultrasound Holography. *Science* **2005**, *310*, 89–92.
37. Tetard, L.; Passian, A.; Venmar, K. T.; Lynch, R. M.; Voy, B. H.; Shekhawat, G.; Dravid, V. P.; Thundat, T. Imaging Nanoparticles in Cells by Nanomechanical Holography. *Nat. Nanotechnol.* **2008**, *3*, 501–505.
38. Tetard, L.; Passian, A.; Thundat, T. New Modes for Subsurface Atomic Force Microscopy through Nanomechanical Coupling. *Nat. Nanotechnol.* **2010**, *5*, 105–109.
39. Verbiest, G. J.; Simon, J. N.; Oosterkamp, T. H.; Rost, M. J. Subsurface Atomic Force Microscopy: Towards a Quantitative Understanding. *Nanotechnology* **2012**, *23*, 145704.
40. Spitzner, E.-C.; Riesch, C.; Magerle, R. Subsurface Imaging of Soft Polymeric Materials with Nanoscale Resolution. *ACS Nano* **2011**, *5*, 315–320.
41. Spitzner, E.-C.; Riesch, C.; Szilluweit, R.; Tian, L.; Frauenrath, H.; Magerle, R. Multi-Set Point Intermittent Contact (MUSIC) Mode Atomic Force Microscopy of Oligothiophene Fibrils. *ACS Macro Lett.* **2012**, *1*, 380–383.
42. Solares, S. D.; Chawla, G. Exploration of AFM Imaging Artifacts Occurring at Sharp Surface Features When Using Short Carbon Nanotube Probes and Possible Mitigation with Real-Time Force Spectroscopy. *J. Manuf. Sci. Eng.* **2010**, *132*, 030904.
43. Solares, S. D.; Chang, J.; Seog, J.; Kareem, A. U. Utilization of simple scaling laws for modulating tip-sample peak forces in atomic force microscopy characterization in liquid environments. *J. Appl. Phys.* **2011**, *110*, 094904.
44. Ebeling, D.; Solares, S. D. Amplitude Modulation Dynamic Force Microscopy Imaging in Liquids with Atomic Resolution: Comparison of Phase Contrasts in Single and Dual Mode Operation. *Nanotechnology* **2013**, *24*, 135702.
45. Tamayo, J.; Garcia, R. Effects of Elastic and Inelastic Interactions on Phase Contrast Images in Tapping-Mode Scanning Force Microscopy. *Appl. Phys. Lett.* **1997**, *71*, 2394–2396.
46. Bar, G.; Delineau, L.; Brandsch, R.; Bruch, M.; Whangbo, M. Importance of the Indentation Depth in Tapping-Mode Atomic Force Microscopy Study of Compliant Materials. *Appl. Phys. Lett.* **1999**, *75*, 4198–4200.
47. San Paulo, A.; Garcia, R. Amplitude, Deformation and Phase Shift in Amplitude Modulation Atomic Force Microscopy: A Numerical Study for Compliant Materials. *Surf. Sci.* **2001**, *471*, 71–79.
48. Williams, J. C.; Solares, S. D. Towards 4-Dimensional Atomic Force Spectroscopy Using the Spectral Inversion Method. *Beilstein J. Nanotechnol.* **2013**, *4*, 87–93.
49. Thangawng, A. L.; Ruoff, R. S.; Swartz, M. A.; Glucksberg, M. R. An Ultra-Thin PDMS Membrane As a Bio/Micro-Nano Interface: Fabrication and Characterization. *Biomed. Microdevices* **2007**, *9*, 587–595.